ORNL/TM-2022/2619

Performance of Microreactor Test Article with Embedded Sensors during Testing in the Single Primary Heat Extraction and Removal Emulator

Holden C. Hyer
Daniel C. Sweeney
Christian M. Petrie
Jeremey L. Hartvigsen
Zachary D. Sellers
Troy C. Unruh
Timothy L. Phero

September 2022

OAK RIDGE National Laboratory

ORNL IS MANAGED BY UT-BATTELLE LLC FOR THE US DEPARTMENT OF ENERGY

ORNL/TM-2022/2619

Nuclear Energy and Fuel Cycle Division

PERFORMANCE OF MICROREACTOR TEST ARTICLE WITH EMBEDDED SENSORS DURING TESTING IN THE SINGLE PRIMARY HEAT EXTRACTION AND REMOVAL EMULATOR

Holden C. Hyer (ORNL)
Daniel C. Sweeney (ORNL)
Christian M. Petrie (ORNL)
Jeremey L. Hartvigsen (INL)
Zachary D. Sellers (INL)
Troy C. Unruh (INL)
Timothy L. Phero (INL)

September 2022

Milestone #: M3AT-22OR0804011

Prepared by
OAK RIDGE NATIONAL LABORATORY
Oak Ridge, TN 37831-6283
managed by
UT-BATTELLE LLC
for the
US DEPARTMENT OF ENERGY
under contract DE-AC05-00OR22725

TABLE OF CONTENTS

LIST OF FIGURES

ACKNOWLEDGMENTS

This work is supported by the Microreactor Program of the US Department of Energy's (DOE)'s Office of Nuclear Energy. Embedded fiber-optic sensor fabrication and testing was originally sponsored by the Laboratory Directed Research and Development program of Oak Ridge National Laboratory, which is managed by UT-Battelle LLC for DOE. Dan King, Adam Hehr, and Mark Norfolk of Fabrisonic LLC performed the sensor embedding. Holly Trellue of Los Alamos National Laboratory provided the 3D printed hex block for sensor embedding.

ABBREVIATIONS

AM	additive manufacturing
DOE	US Department of Energy
FEA	finite element analysis
INL	Idaho National Laboratory
OBR	Optical Backscatter Reflectometer
ORNL	Oak Ridge National Laboratory
SPHERE	Single Primary Heat Extraction and Removal Emulator
SS	stainless steel
TC	thermocouple
UAM	ultrasonic additive manufacturing

EXECUTIVE SUMMARY

The nuclear industry is pursuing microreactors that can be factory assembled and deployed to remote regions for reliable power generation. One class of microreactors uses a monolithic metal core block coupled to heat pipes that use passive heat flow, increasing the surface area for heat transfer without requiring active coolant flow through the reactor core. Additional experimental testing is required to understand the heat rejection limitations of heat pipes and thermal stresses in the monolithic core block due to significant temperature gradients. This report describes the initial characterization and testing of a stainless-steel test article that was fabricated with embedded sensors to measure heat pipe performance limits, as well as spatially distributed temperatures and strains during electrically heated thermal testing to simulate nuclear heating. The electrically heated testing was performed in the Single Primary Heat Extraction and Removal Emulator facility located at Idaho National Laboratory. The ultimate goals of this work are to (1) accurately monitor temperature and strain distributions that result from differential thermal expansion in the test articles and (2) quantify the heat rejection limits of heat pipes as a function of operating temperature and working fluid during steady-state and transient operations. Initial tests focused on the feasibility of using advanced fiber-optic sensors and other sensor technologies to improve the understanding of temperature and strain distributions within the electrically heated experiments. However, these sensing capabilities could benefit the broader microreactor community if the sensors could be used to monitor component and system health during nuclear operations to inform a limited number of microreactor operators, ultimately reducing operation and maintenance costs and moving toward semiautonomous operation.

1. INTRODUCTION

Microreactors with a thermal power output in the range of 0.1 to 20 MW that can be easily assembled in a factory are desired to provide power generation in remote areas [1]. Microreactor concepts generally include passive safety features with the ability to reach high temperatures to increase thermal efficiencies [2, 3]. Various reactor coolants are being considered, including flowing He, molten salt, and light-water reactor designs [4]. Other microreactor concepts are taking advantage of passive heat removal capabilities using heat pipes, which leverage the boiling and condensing of a molten metal to transport heat from the core to a heat sink, effectively eliminating the need for any forced circulation within the core [2, 3].

Heat pipes are typically designed as enclosed cylinders filled with a high vapor pressure metal, such as Na or K. As the metal is vaporized near the fueled region in the core (i.e., hot end), the vapor circulates toward the cold end where heat is transferred over a large surface area to a heat sink. The metal then flows back down through a porous wick located on the inner surface of the pipe via capillary action, as shown in Figure 1(a). A Na-filled heat pipe usually operates most efficiently at ~650°C [5], and a properly designed heat pipe operates under near-isothermal conditions. However, there is a limit to how much heat or heat flux can be rejected from a heat pipe, depending on the working fluid and the operating temperature [5]. These thermal limits are based on (1) sonic velocity limits at the evaporator exit, (2) capillary flow limitations in the wick, (3) entrainment counterflow limits, and (4) boiling and local dryout near the wall [5].

Heat rejection can also cause significant thermal stress in the monolithic metal core used to house the fuel and heat pipes. If the thermal stresses are too significant, a heat pipe could warp and de-bond from the core block, reducing its heat rejection capabilities and requiring the neighboring heat pipes to compensate for the additional heat rejection. Moreover, the overloading that occurs after one heat pipe fails could cause cascading failure. Therefore, it is necessary to understand the fundamental heat rejection limitations of heat pipes as a function of operating temperature and working fluid, as well as the thermal stresses generated in the core block during reactor operation. In a previous report, finite element analysis (FEA) modeling was used to predict the temperature differences in a microreactor hex block test article [6]. As shown in Figure 1(b), the temperature differences between the center of the hex block where the heat pipe is located and the outer regions of the pipe are estimated to be ~70°C, assuming that the system is perfectly insulated. The simulated results provide good insight into how the system behaves, but the temperature variations could change significantly in an experimental setup, especially if the system is poorly insulated. Thus, detailed mappings of temperature and strain within heat pipes and their surrounding test articles during representative internal heating are required at temperatures ranging from 500 to 700°C.

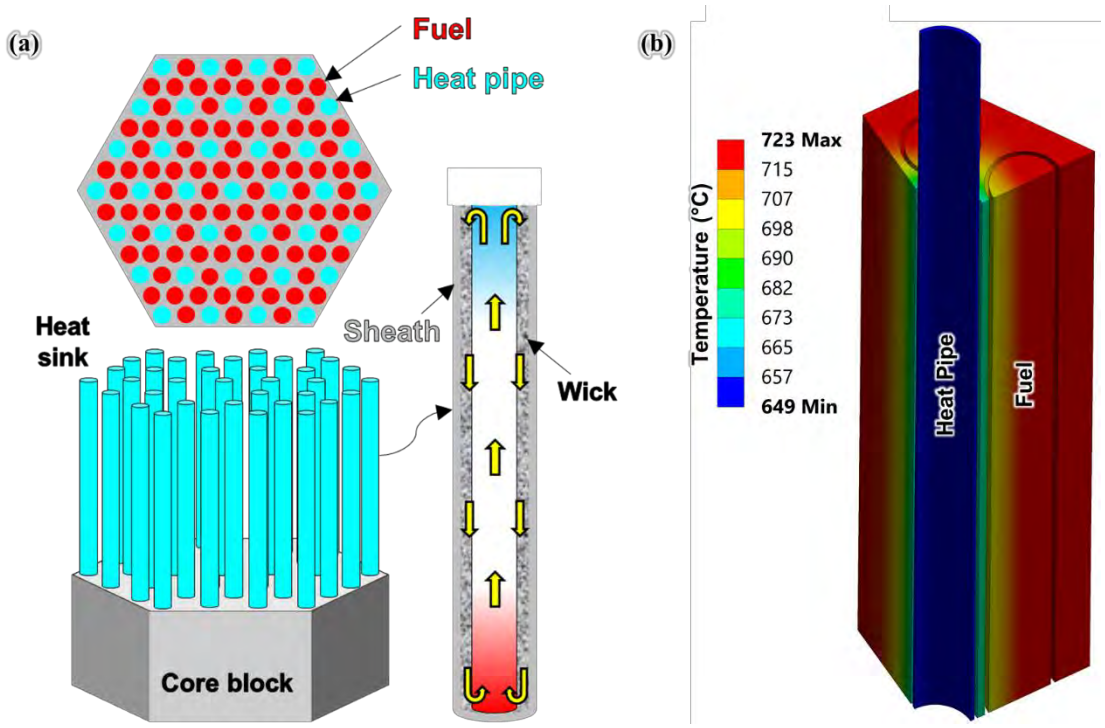

Figure 1. (a) Schematic of a heat pipe–based reactor and the general flow of the working fluid inside the sheath of a heat pipe; (b) FEA model of the temperature distributions (°C) within the monolithic stainless-steel (SS) block that surrounds one heat pipe during electrically heated thermal testing [6]. The temperature differences between the heat pipe and the outer portion of the core block are expected to be ~70°C for a perfectly insulated hex block and a total thermal power of ~1,900 W.

Traditionally, temperature and thermal strain would be monitored using thermocouples (TCs) and resistive strain gauges, respectively. However, these sensors provide measurements at only one location, which limits the ability to realistically map the entire temperature distribution within the heat pipes and monolithic test article. Furthermore, resistive strain gauges are not typically rated to withstand the temperatures that are being considered for heat pipe–based microreactors. Fiber-optic sensors are a promising technology for measuring temperature and strain distributions during either electrical or nuclear heating due to their ability to operate at high temperatures (>1,000°C) [7-10] and moderate radiation dose [9-11]. Furthermore, temperature and strain can both be continually measured along the length of the entire fiber [7, 12]. However, for accurate strain measurements, the fiber must have adequate mechanical coupling with the component. Ideally, the fiber-optic sensors could be directly embedded and bonded within the surrounding metal matrix [12-17], thus eliminating concerns related to the degradation of adhesives at high temperatures or under irradiation. Typically, SS316L and SS304 are chosen for the core block materials because of their relatively high strength, corrosion resistance, and high commercial availability [18, 19]. However, conventional SS processing via casting and subsequent working is not ideal for embedding fragile fiber optics. Therefore, recent studies have used additive manufacturing (AM) to rapidly prototype new component designs with geometric complexities [20, 21] and embed fiber-optic sensors during the fabrication process [12, 15, 16, 22-25].

A hex block test article was previously manufactured with embedded TCs and fiber-optic sensors for strain and temperature monitoring during thermal testing at the Single Primary Heat Extraction and Removal Emulator (SPHERE) facility at Idaho National Laboratory (INL) [1, 6]. SPHERE is a nonnuclear test bed that uses electric cartridge heaters to simulate thermal loads expected from fuel during microreactor operation. The hex block was intentionally designed to house the cartridge heaters

surrounding one Na-based heat pipe for heat extraction. This report summarizes the results recorded from embedded and nonembedded sensors used to map the strain and temperature distributions within the hex block. Thermal cycling around the operational temperature of the heat pipe (600–675°C) was performed to simulate possible power variations and fluctuations in the core and determine the overall efficiency in heat rejection of the heat pipe.

2. EXPERIMENTAL METHODS

2.1 SENSOR SELECTION

Fused silica fiber optics (IVG Fiber) with a Ge-doped silica core, pure silica cladding, and a Cu coating were used to measure distributed strain in the hex block. A Cu coating was chosen over more typical polymer coatings because of its high melting temperature. Nonembedded polyimide coated fibers (Fibercore) were also chosen for distributed temperature measurements. More information on the fibers can be found in previous reports [6, 24]. Additionally, Type K TCs (Omega Engineering) and a high-temperature strain gauge (Kyowa Electronic Instruments) were chosen to compare the temperature and strain measurements recorded by the fibers. The high-temperature strain gauge was housed in a ~2 mm SS sheath and has a gauge length of 2 cm. The recommended operating temperature for the strain gauge was <500°C, so this sensor was not expected to provide reliable data at the highest operating temperatures.

2.2 SENSOR PLACEMENT

The hex block test article was fabricated from SS316L powder feedstock using a M400-4 laser powder fusion system from Electro-Optical Systems at Los Alamos National Laboratory. The hex block was designed with seven through holes, one located in the center for the heat pipe, and six others located ~18 mm from the center that housed the cartridge heaters used to simulate the thermal loads from nuclear fuel. More information on the design and fabrication of the test article can be found in previous reports [1, 6, 24].

Ultrasonic AM (UAM) was used to embed the fiber-optic and TC sensors in the hex block. UAM is a solid-state (i.e., does not involve melting) process that uses a tooling called a *sonotrode*, which operates at a desired ultrasonic frequency of ~20 kHz [26]. In combination with an applied force, the sonotrode is rolled with a scrubbing motion to ultrasonically weld thin metal foils together. UAM is typically a hybrid process that couples the ultrasonic welding with computer numerical control machining for milling operations. During the sensor embedding process, channels were machined on one of the flat surfaces of the hex block (Figure 2[a]). Two TCs along with two optical fibers were laid within the channels and ultrasonically welded over the top with SS304 foils. The TCs were embedded first, and then the channels for the fibers were machined. Additional larger channels were machined parallel to the embedded fibers (Figure 2[a]) but were left vacant so that extra fibers could be inserted to compare an embedded fiber with a “floating” fiber. Multiple foils were welded over the top of the sensors, as shown in Figure 2(b), leaving the final part shown in Figure 2(c). The location of the sensors is shown in Figure 3(a). The embedded TCs were labeled “Embedded TC 1” and “Embedded TC 2,” as shown in Figure 3(b). Only of the embedded fibers survived the UAM process. More information on the UAM and fabrication process can be found in previous reports [6, 24, 25].

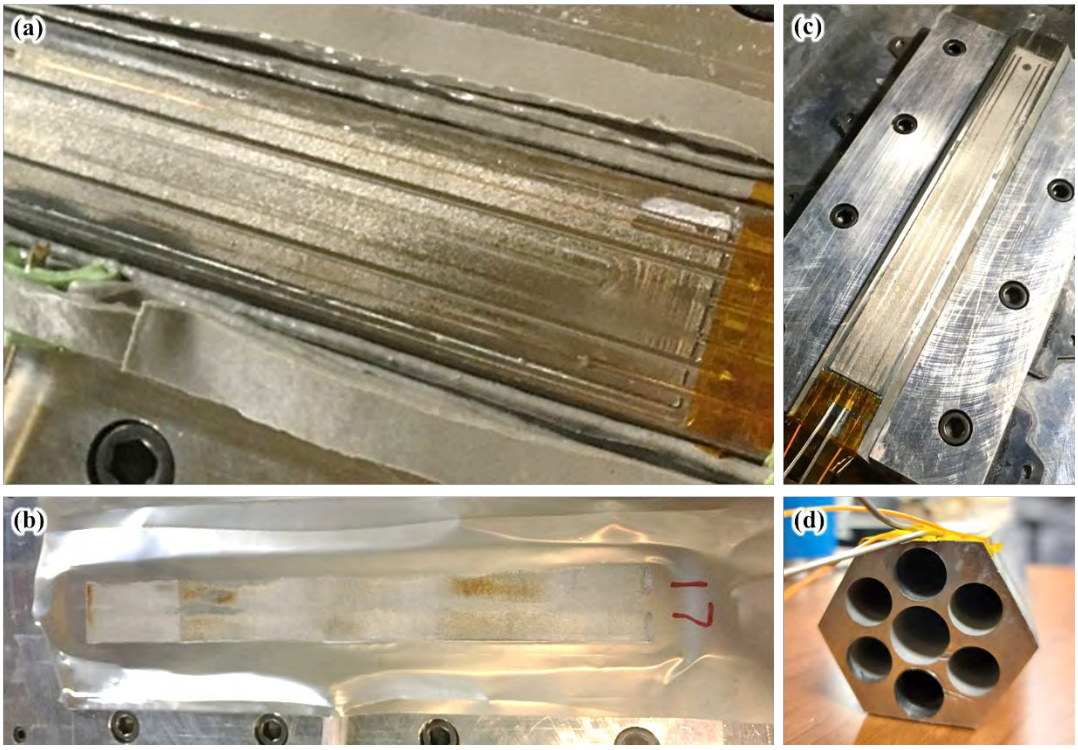

Figure 2. (a) The channels used to sequester the sensors while (b) a foil is welded over the top. (c) After successive welds, the edges of the foil that are unwelded were trimmed. Initially, the surface with the embedded sensors was milled down, thereby making the embedded sensors closer to the cartridge heaters than any sensor placed on the outer surfaces as shown in (d).

Additionally, a high-temperature stain gauge was attached to the face adjacent to the one with the embedded fiber by spot-welding the SS304 flange containing the sensitive portion of the gauge to the hex block with thin Ni-Cr foils over the top of the cabling for strain relief, as shown in Figure 3(b). Three nonembedded TCs were spot-welded to the surface of the face adjacent to the face containing the embedded sensors but opposite the face that contains the strain gauge. The spot-welded TCs labeled “Surface TC 1,” “Surface TC 2,” and “Surface TC 3” in Figure 3(a) were located at axial positions -25, 0, and 230 mm using the coordinate system shown in Figure 3(b). Figure 4 shows a transverse cross-sectional view through the region in which the fiber optic sensors were embedded to better illustrate the locations of all sensors. The embedded TCs were closer to the heaters than the embedded or floating fibers and the surface TCs.

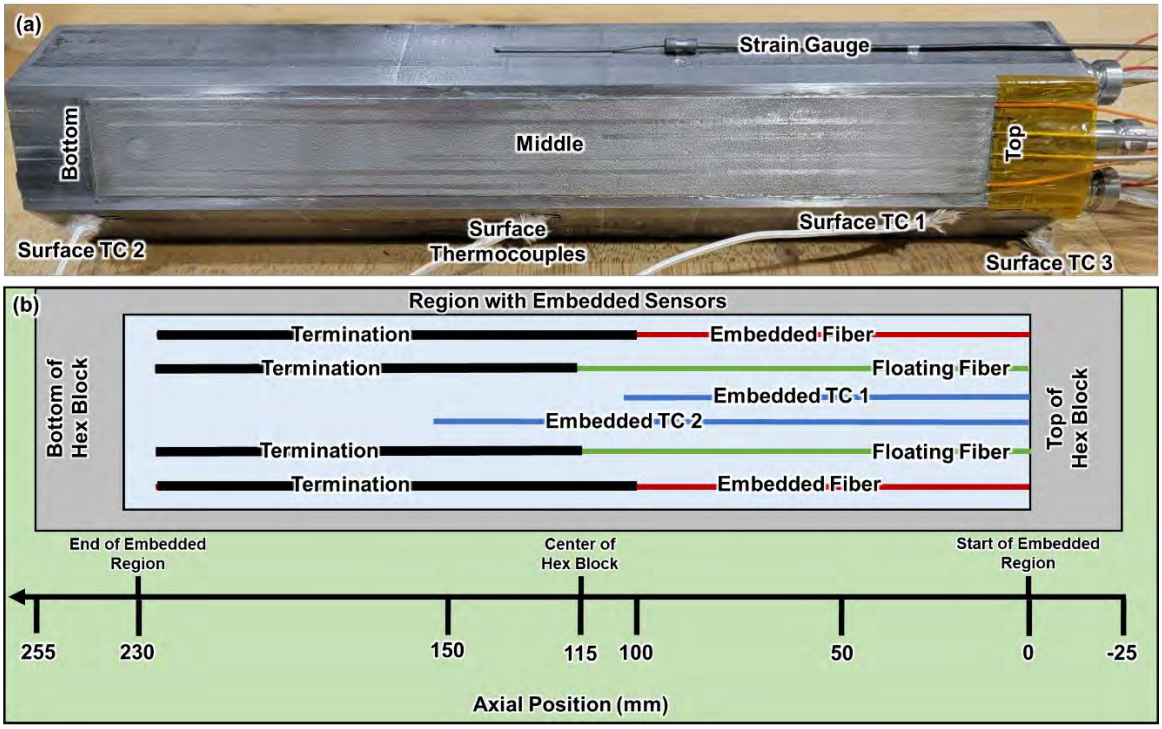

Figure 3. (a) Photo and (b) schematic of the sensor placement along the hex block test article. The red/green segment of the embedded/floating fibers indicates useable sensing range. The black banding at the end of the fiber indicates the termination in which no sensing data can be acquired. The hex block is 280 mm long, and the embedded region is situated 25 mm from either end of the block.

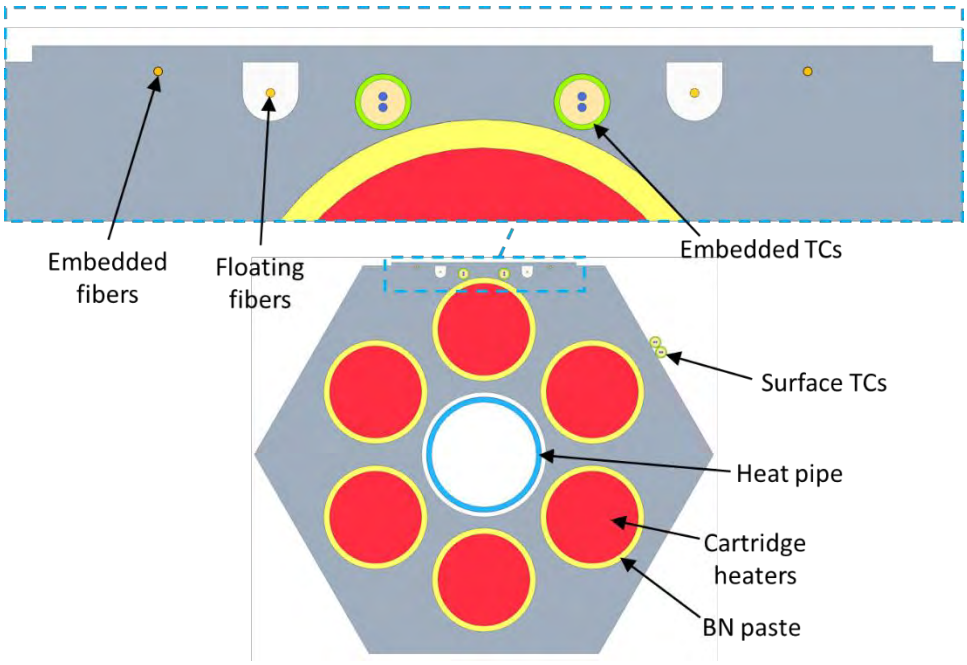

Figure 4. Transverse cross-sectional view showing the positioning of all sensors.

2.3 SPHERE SETUP AND TESTING

SPHERE is a nonnuclear test bed designed to test core block components with one heat pipe under varying steady-state and transient thermal loads. A SS316 cylindrical chamber was chosen to house the microreactor test article; the chamber can hold a high vacuum and pump and purge the system with inert gases, such as He, N_2, or Ar. Cartridge heaters were used to simulate the expected heat loads from the nuclear fuel. The test bed can provide up to 20 kW of electrical power to the cartridge heaters, which can reach a maximum temperature of ~750°C. Flowing chilled water, sourced by a 2.5 kW chiller, was used to cool the top end of the heat pipe that extended away from the test article. A gas-gap calorimeter was placed in the cooling water loop to measure the heat rejection and determine how much heat was removed from the heat pipe compared with what was being supplied to the cartridge heaters. More information on the assembly and capabilities of SPHERE can be found in previous reports [1, 2, 27].

The hex block with embedded fibers was fitted with six cartridge heaters and one Na-filled heat pipe. Boron nitride thermal paste was used to fill the cavities between the cartridge heaters and the holes in the hex block. TCs were placed in the center of each cartridge heater to ensure that their temperature limitations were not exceeded. The strain gauge and nonembedded TCs were then fixed to the outside surfaces of the hex block. Afterward, the block was wrapped in insulation to reduce thermal losses to the surrounding environment. The chamber was pumped down to a pressure of 10^{-4} torr and purged with N_2 five times before backfilling with N_2 and holding the pressure at ~765 torr (0.1 psig) during the testing. The temperature profile used in the experiment (Figure 5) was performed over 24 h while ensuring that the heat pipe's maximum operating temperature of 650°C was not exceeded. Initially, the cartridge heaters were ramped to 200, 400, 500, and 600°C and held for 30–60 min at each temperature. Once at 600°C, the temperature was cycled from 600°C to 625, 650, and 675°C and held for 1 h at each temperature before cooling to 600°C and holding for 1 h before the next cycle. Finally, the temperature was held at the heat pipe's operating temperature of 650°C for 4 h before cooling the system to room temperature.

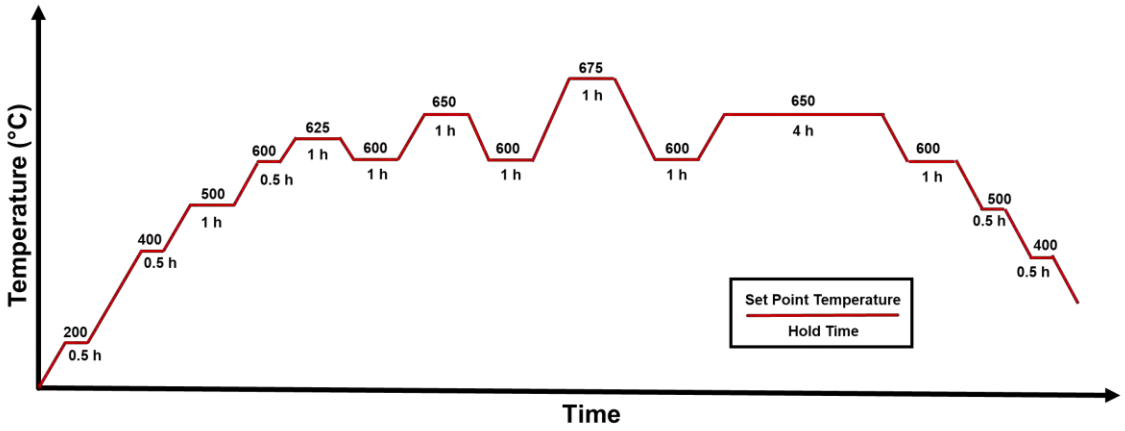

Figure 5. Temperature profile of the 24 h period in which the hex block was subjected to various thermal loads.

2.4 SENSOR INTERROGATION

The fibers were interrogated with an Optical Backscatter Reflectometer (OBR) 4600 (Luna Innovations), which relies on the Raleigh backscattering of light that is delivered by a tunable laser. Using optical frequency domain reflectometry, scattering centers along the fiber can be spatially interrogated along the length of the fiber. During interrogation, the backscattered light is combined with a reference beam, producing an interference pattern. The beat frequencies of the interference spectra can be analyzed using Fourier transforms to discretize the spectral data within specific spatial regions, or gauges, along the fiber. Cross-correlations can be performed with reference spectra collected under nominal conditions (e.g., room temperature, unstrained) to quantify spectral shifts. This is analogous to what occurs with a fiber Bragg grating, which are artificially etched gratings that provide stronger reflections sights than scattering centers in fibers with no fiber Bragg gratings. The spectral shift ($\Delta\nu$) can be calibrated to a change in temperature (ΔT) or strain (ε):

$$\frac{\Delta\nu}{\nu} = K_T \Delta T + K_\varepsilon \varepsilon, \tag{1}$$

where K_T and K_ε are constants that determine the fiber's sensitivity to temperature and strain, respectively. For a nonembedded fiber, the contribution to the $\Delta\nu$ due to mechanical strain will be 0, thus the $\Delta\nu$ will be function of ΔT and K_T. The temperature coefficient K_T is equal to the sum of the thermal expansion of the silica fiber (α_{fiber}) and the thermo-optic coefficient (ξ). Because ξ is dependent on temperature [7], using a constant value for K_T is nonideal. Therefore, this work used a calibration proposed in Wood et al. [28] for a single-mode silica fiber:

$$\Delta T = -1.33E10^{-4}\Delta\nu^2 - 0.748\Delta\nu - 0.229, \tag{2}$$

The embedded fibers in this work were subjected to thermal testing and therefore are exposed to contributions from both temperature and strain. The strain felt by the fiber will be a result of the differential expansion between the fiber and the SS304 matrix:

$$\varepsilon = \left(\alpha_{\text{matrix}}(T) - \alpha_{\text{fiber}}(T)\right)\Delta T. \tag{3}$$

For the case of a homogenous and isotropic strain, K_ε can be simplified to an approximate value of 0.78 based on a lumped parameter that accounts for photoelastic effects [7]. Compensation for the effects of temperature (primarily thermo-optic effects) on the strain measured by the embedded fiber can be made by using a nonembedded fiber that is "floating" in the matrix and will therefore experience only the effects of temperature.

Both the embedded and floating fibers were continuously interrogated over the duration of the test, sampling every 2 min. All fiber data were processed with an adaptive reference scheme in Python 3.8. More information on the reference scheme can be found elsewhere [29-31]. A gauge length of 5 mm and a sensor spacing of 2.5 mm were chosen for spatial discretization. The sensor spacing is implemented for a given spatial range over which the data along the gauge length are interpolated.

Except for the fibers, the SPHERE environment was controlled and the sensor data were logged using a Labview program. This program controlled the temperature of the cartridge heaters and monitored the heater power, temperature changes in the coolant that flowed through the gas-cap calorimeter, temperatures from the various TCs, and voltage changes from the strain gauge. Using the measured coolant flow rate, evaluated specific heat capacity, and measured temperature change recorded from the gas-cap calorimeter, the extracted power was computed to quantify the amount of heat being removed by

the heat pipe. Voltages from the strain gauge were converted to a strain using a temperature-dependent gauge factor that varied between 1.71 and 1.87, as recommended by the manufacturer.

3. RESULTS

3.1 STRAIN MEASUREMENTS

At the top of the hex block, the embedded sensors were routed out from the embedded region, as shown in Figure 3(a). The sensors can easily be strained at the entrance to the embedded region during handling, making it a potential failure point—something that was indicated in previous work [15, 16, 25]. Before ramping to the heat pipe's operational temperature range (>600°C), a series of lower temperature holds were performed at 200, 400, and 500°C to allow the part to reach a uniform temperature and potentially relieve any stress in the fiber at the entrance to the embedded region.

In addition to measuring spectral shifts that can be correlated to changes in temperature or strain, the OBR can also measure the intensity of the backscattered light as a function of position along the fiber. This is useful for determining large reflections or breaks in the fiber that may occur during setup or thermal testing. The end of the fiber is terminated to prevent large back reflections at the fiber/air interface at the end of the fiber. This is typically accomplished using either a coreless optical fiber with a refractive index similar to that of the fiber cladding or—for lower temperature applications—using an index-matching gel. Matching refractive index prevents excessive light bleeding. Prevention of this large reflection is required from obscuring significant portions of the backscattered signals occurring along the length of the fiber that are used for sensing near the end reflection. The length of the termination must be long enough (typically >100 mm) so that the light that enters the termination fiber does not couple back into the single-mode fiber under test. For the embedded fibers, a ~115 mm long coreless termination was spliced on to the Cu-coated fiber. An oversized channel was machined before embedding the fibers to accommodate the 115 mm long termination. The 100 mm embedded fiber region was located immediately upstream of the termination.

Strain recorded from the embedded fiber is spatially mapped in Figure 6(a). The spatial position is plotted along the *y*-axis. Positions are plotted relative to the entrance of the embedded region, as indicated in Figure 3(b), and increasing positions are located closer to the bottom of the hex block. As the hex block was heated to 200°C, the SS304 matrix expanded more than the fused silica fiber, resulting in relatively uniform increases in tensile strain within the embedded region of the fiber. Outside the embedded region there is no mechanical strain on the fibers, but an effective "strain" is recorded primarily due to thermo-optic effects (Eq. [1]). Unfortunately, the fiber failed prematurely near time 140 min. The reflected signal amplitudes measured in the embedded fiber are shown in Figure 6(b) before the heating started at 0 min and near 140 min when the fiber failed. In these plots, the position along the *x*-axis is the same as the position along the *y*-axis in Figure 6(a). At 0 min, the reflected signal amplitude is fairly uniform for all positions until it drops off sharply at ~100 mm where the termination starts. At 140 min, a large back reflection is observed at ~0 mm, which corresponds to the start of the embedded region. The fiber appears to have broken at the high strain point where the fiber was routed out of the embedded region. Similar failures have been observed in previous tests, which have since motivated improved methods for routing fibers out of the embedded region. The test articles that were evaluated in this report were fabricated in fiscal year 2020 before these issues were identified.

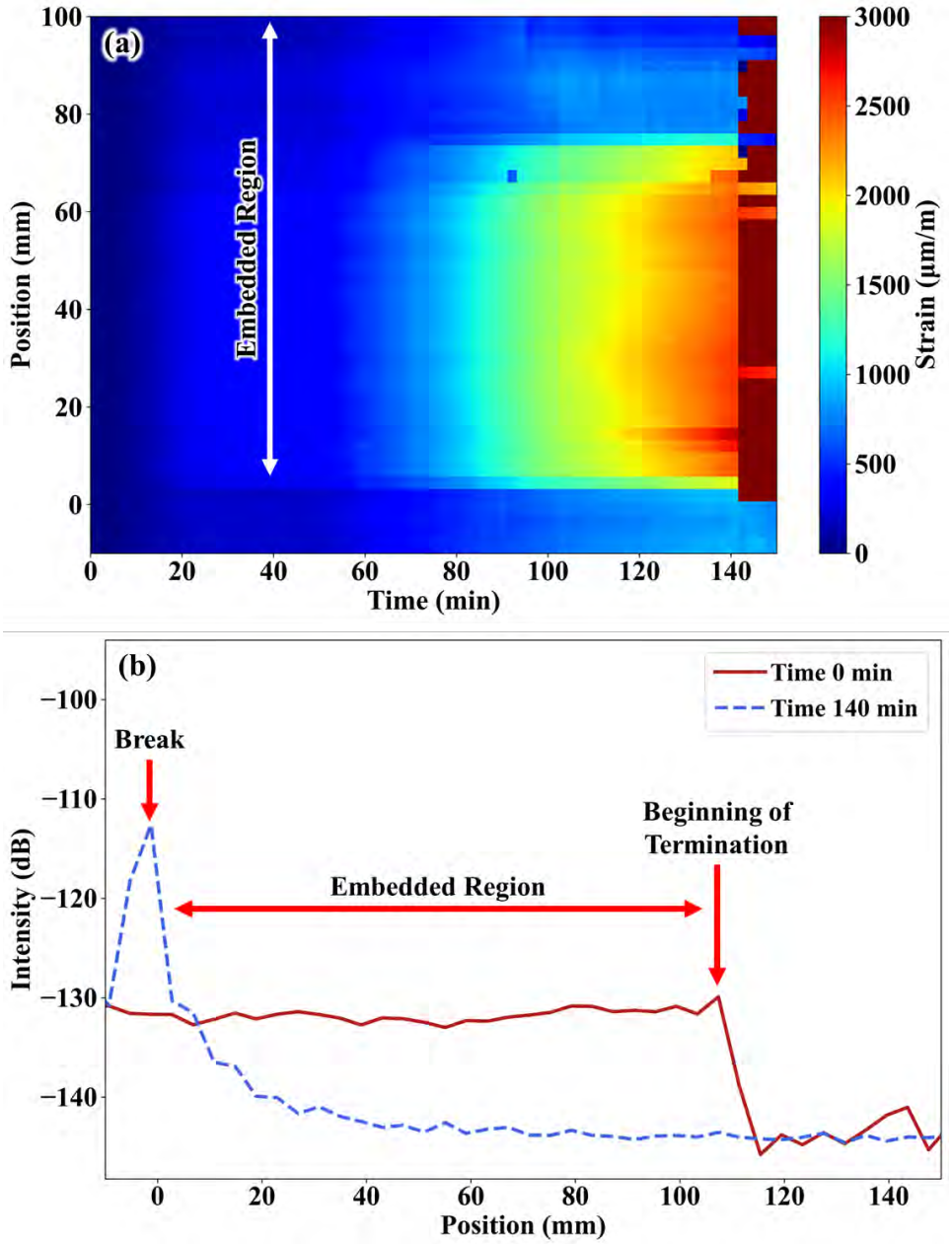

Figure 6. (a) Strain from the embedded fiber mapped spatially along the length of the fiber in the region where the fiber was embedded. Fiber strains up to 3,000 μm/m were measured before the fiber failed at ~140 min. (b) Reflected signal intensities measured vs. the position along the fiber before heating b (0 min) and at 140 min (after the fiber failed). The break was observed at the entrance to the embedded region and was not in the embedded region.

Along with the embedded fiber, additional larger cavities (Figure 2[a] and Figure 4) were machined into the hex block to allow a nonembedded fiber to be inserted. Because the nonembedded fiber was floating in the matrix, it was not subjected to mechanical strain and responded only to changes in temperature. The temperature recorded from the floating fiber is mapped in Figure 7(a) using the calibration in Eq. (2) from Wood et al. [28]. The floating fiber measured significant changes in temperature over ~120 mm. This fiber was inserted with the end of the fiber positioned near the bottom of the hex block (Figure 3). Because of the required fiber termination length, the temperature could be resolved only over a smaller

region of the test article. The measured temperatures are highest above ~100 mm. The temperature between ~0 and 100 mm is relatively uniform with respect to position. Below ~0 mm (i.e., moving toward the top of the test article), the temperature decreases moving further from the test article and the cartridge heaters.

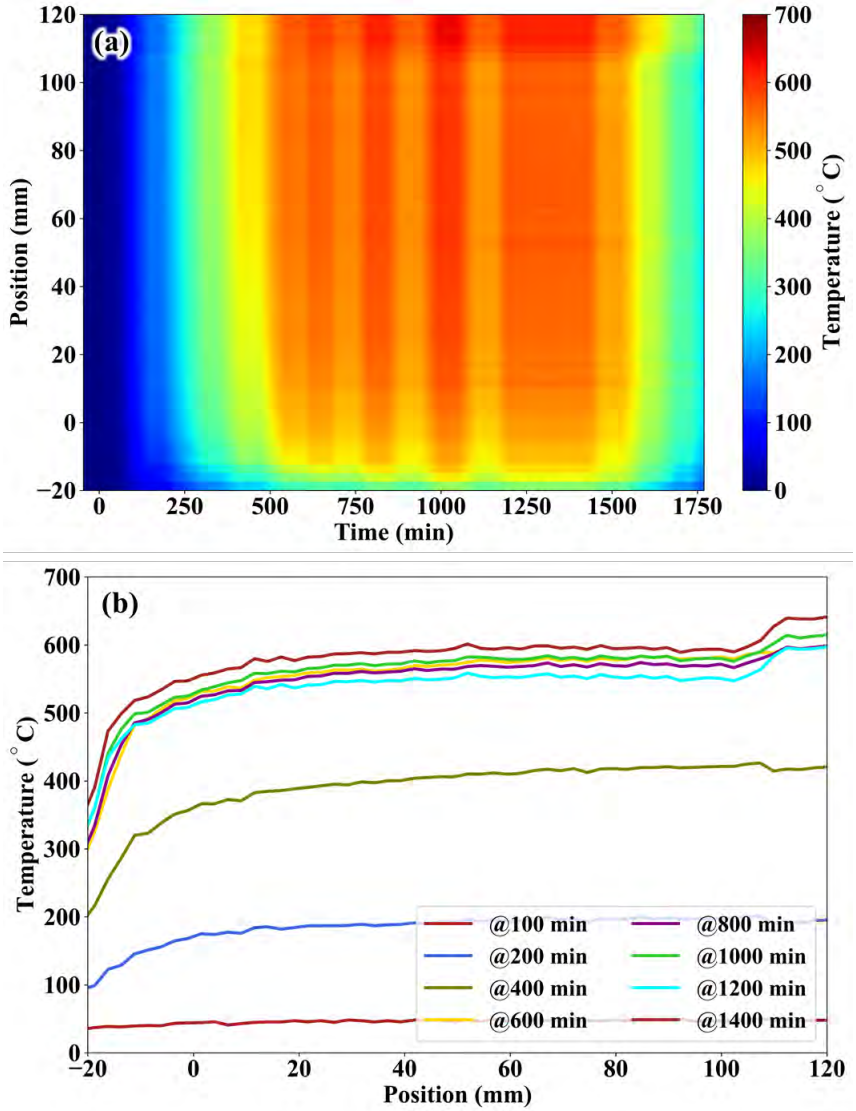

Figure 7. (a) Temperature recorded by the floating fiber spatially mapped over the duration of the heating (b) at specific times during the heating.

Besides the ~30°C increase in temperature near 100 mm, the spatial temperature variations appear to be relatively minor with only slight decreases in temperature due to axial heat losses. Figure 7(b) shows 2D plots of the spatial temperature profiles at various times during the heating. The increases in temperature near 100 mm may be a result of nonuniform heat generation within the cartridge heaters or variations in insulation or other factors that would affect heat rejection within the block.

The strain measured by the embedded fiber includes contributions from temperature and strain, as expressed in Eq. (1). Because a floating fiber only observes changes in temperature, it can be used to compensate the strain that the embedded fiber recorded. The fiber strain shown in Figure 8 is the compensated strain in the embedded fiber determined after subtracting the floating fiber strain. Based on

Eq. (3), the expected thermal strain due to the changes in thermal expansion from the expanding masses during heating was plotted along with the compensated fiber strain, showing relatively good agreement before fiber failure. Therefore, even though the fiber failed prematurely at the entrance to the embedded region, it was properly bonded and exhibited adequate strain coupling.

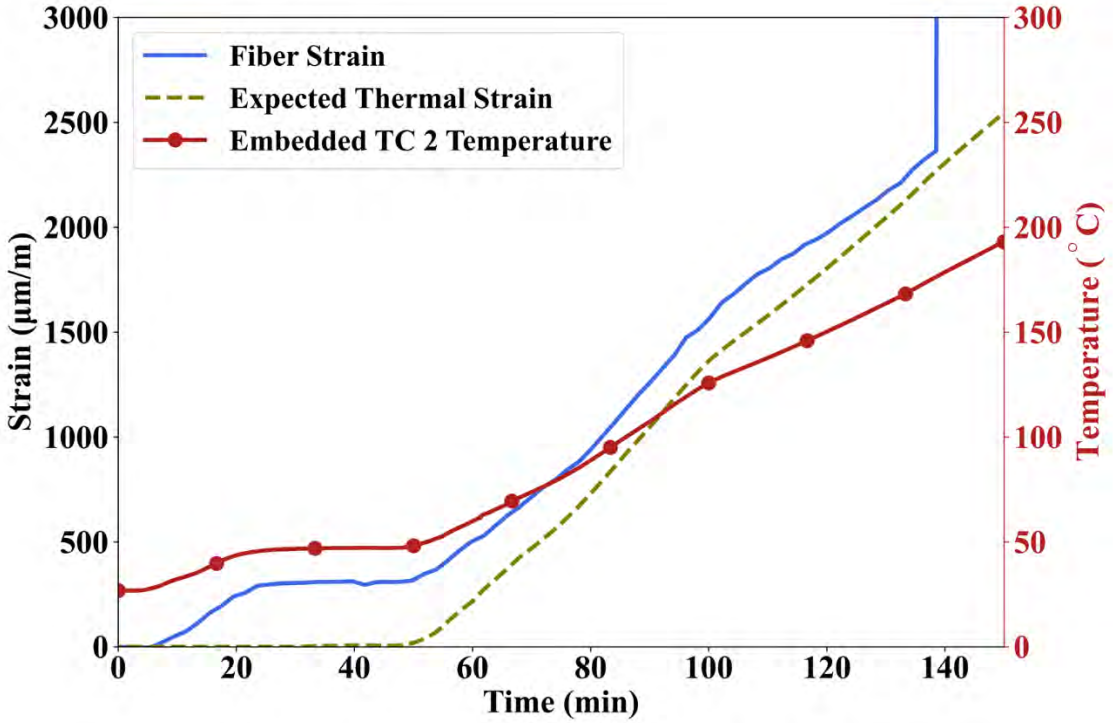

Figure 8. Strain recorded by the embedded fiber compared with expected thermal strain due to the difference in thermal expansion between the fiber and the SS304 matrix.

A high-temperature resistive strain gauge with a recommended operating temperature <500°C was also fixed to the hex block for strain measurements. The strain recorded from the strain gauge is shown in Figure 9. The plotted strains are difficult to interpret because the vendor does not provide much detail regarding the materials, properties, and internal geometry of the strain gauge. This complicates any modeling that could be performed to estimate differential thermal expansion between the strain gauge and the SS304 block. Nevertheless, the strain should generally follow the temperature. Below the recommended operating temperature of the resistive strain gauge (<500°C), strain generally follows the temperature. At higher temperatures, the strain gauge experiences thermal drift, as evidenced by the time variations in the measured strain when the temperature is held constant. Although the calibration factor was applied, it is difficult to quantify the expected strain for the strain gauge. Based on the thermal expansion of SS304, the maximum strain at 675°C would be ~11,300 μm/m, which is significantly lower than what the strain gauge shows.

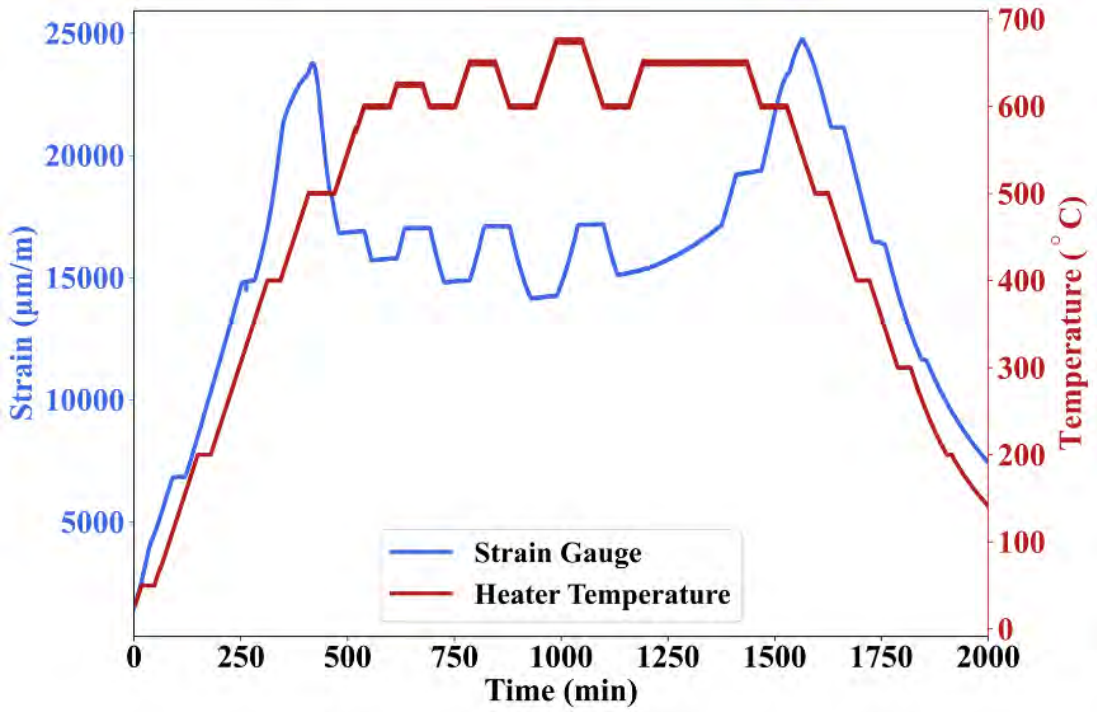

Figure 9. Strain measured by the high-temperature strain gauge.

3.2 MAPPING TEMPERATURE IN THE HEX BLOCK

Even if resistive strain gauges or fiber-optic strain sensors can eventually be used to reliably measure strain in some locations within the hex block, detailed temperature maps are required to determine local strain throughout the hex block. Besides the floating fiber, TCs were used to measure temperatures at various locations in the hex block. All six TCs that were placed in the center of the cartridge heaters read essentially the same temperature (i.e., were equal to the setpoint temperatures shown in Figure 5), which was expected because those TCs were used to control the power input into each cartridge heater. The other TCs in the system were located on or near the surface of the hex block at different axial locations (Figure 4). Figure 10 shows the temperature vs. time profiles for the two embedded TCs, three surface TCs, and floating fiber at a position near the center of the embedded region (50 mm).

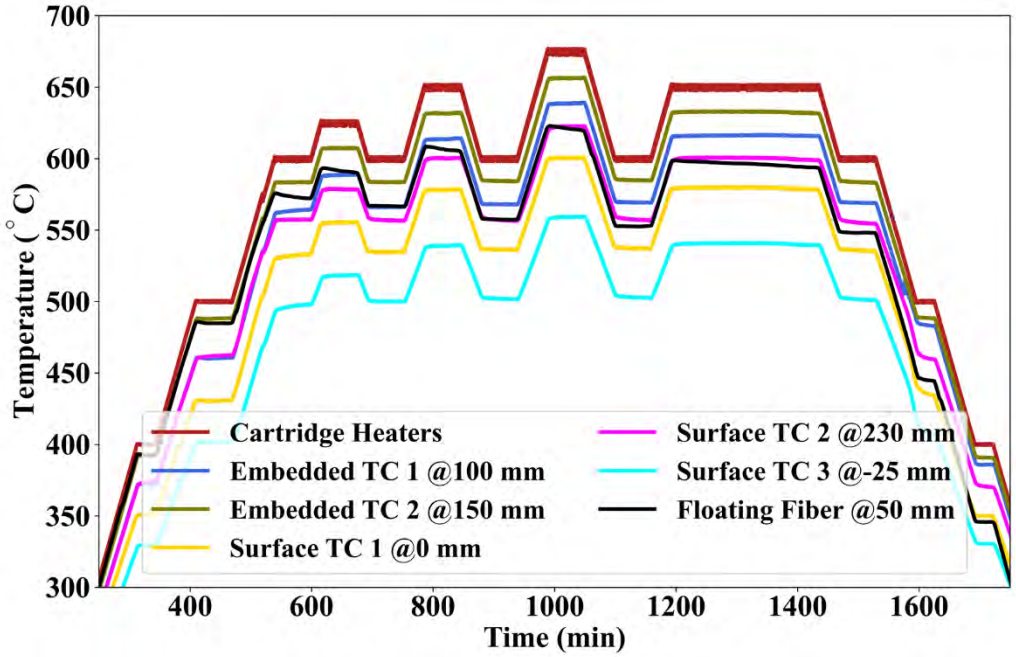

Figure 10. Temperature evolution measured by the floating fiber and the embedded, surface, and heater TCs.

Embedded TC 2 (150 mm), which is located closer to the axial center of the hex block (~140 mm), consistently measures a higher temperature than embedded TC 1 (100 mm). The temperature difference is ~30°C during steady-state operations at temperatures near ~600°C. This is consistent with the floating fiber measuring higher temperatures (Figure 7) at locations beyond ~100 mm. In Figure 10, the floating fiber temperature appeared to drift (i.e., decrease) over time once temperatures were >600°C. Similar drift was observed previously during furnace testing of the same fiber [28], but this drift could be mitigated in future tests by first heat-treating the fiber for an extended duration at ~1,000°C [32].

It is difficult to interpret the spatial variations in temperature based on the time-dependent temperatures shown in Figure 10. Figure 11 shows the axial temperature profiles measured from all sensors at 550, 650, 825, and 1,025 min when the system reached steady state at temperatures of 600, 625, 650, and 675°C, respectively. This figure more clearly shows the consistency between the fiber and the embedded TCs. Thermal drift in the floating fiber may partially explain the slightly lower temperatures measured by the fiber vs. the embedded TCs. At some times, the floating fiber measured significantly different temperatures compared with Surface TC1. The floating fiber and the surface TCs were located on different surfaces of the hex block. Therefore, the discrepancies between the floating fiber and the surface TCs could be caused by azimuthal temperature variations, which are discussed in more detail later in this section.

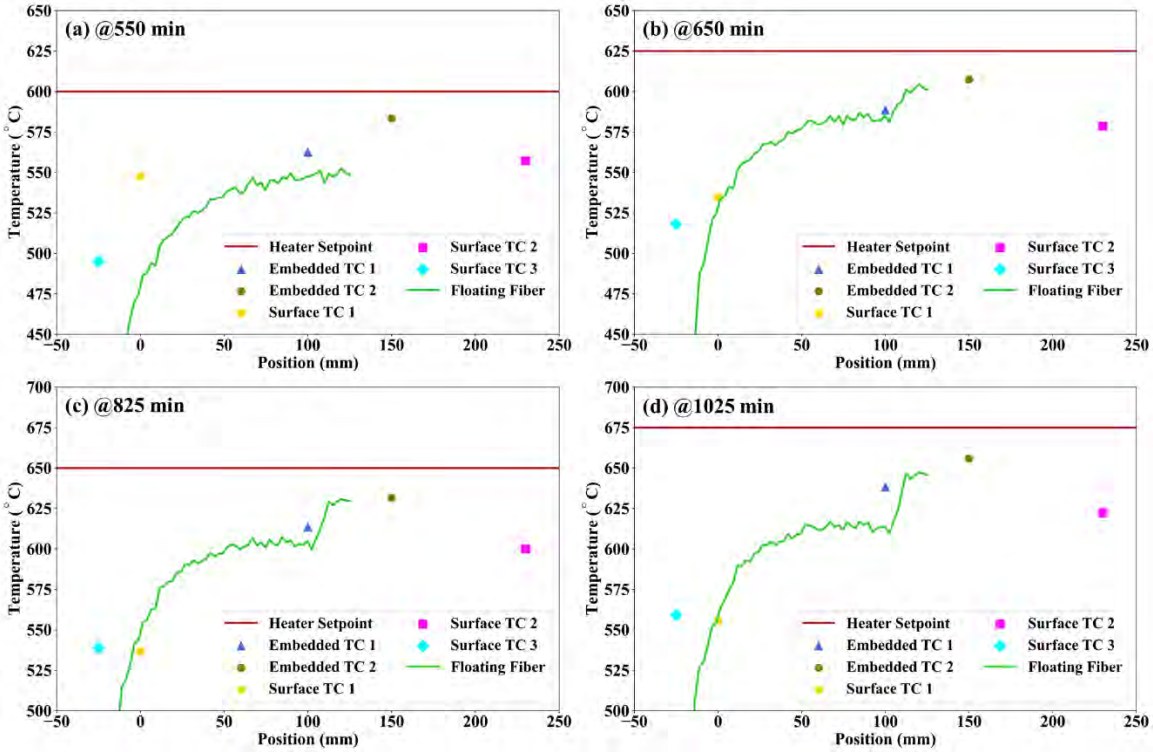

Figure 11. Axial temperature profile determined from all sensor data measured at (a) 550, (b) 650, (c) 825, and (d) 1,025 min corresponding to steady-state temperature set points of 600, 625, 650, and 675°C.

Additional experimental data collected from the gas-gap calorimeter can be used to assess the heat rejected through the heat pipe vs. heat that was rejected radially outward from the hex block. The efficiency of the heat pipe was calculated as the heat rejected to the gas-gap calorimeter divided by the total electrical power supplied to the cartridge heaters, as shown in Figure 12. Heat pipe efficiency data are equal to 0 before ~500 min when the chiller was turned on and after ~1,700 min when the chiller was turned off. During the thermal cycling, only ~20–30% of the energy input into the system was removed through the heat pipe. This low efficiency may have been affected by the lack of BN paste between the hex block and the heat pipe, which increased the thermal resistance between the hex block and the heat pipe and ultimately limited the maximum power that could be reached without exceeding the temperature limitations of the cartridge heaters. The sudden spike and final drop in efficiency ~1600 min is due to chiller power cut-off at this time.

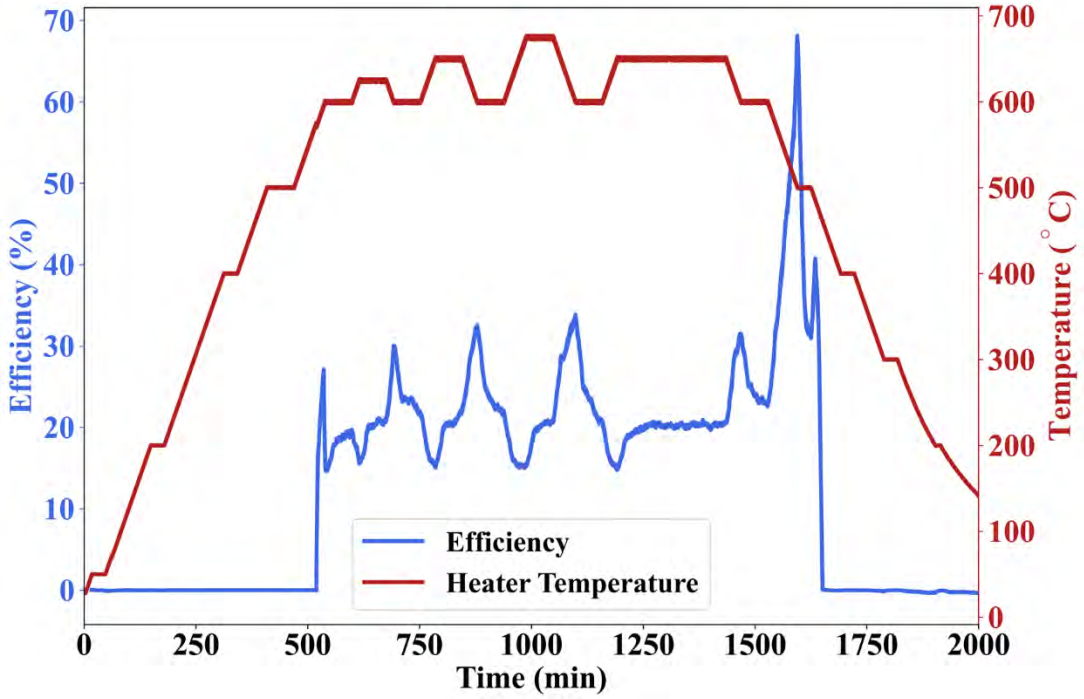

Figure 12. The efficiency of the heat pipe calculated from the total power put into the cartridge heaters vs. what was measured coming out of the cooling water from the gas-cap calorimeter.

The gas-gap calorimeter and the temperatures measured at different radial locations imply that significant heat was being transferred radially outward from the cartridge heaters to the outer surface of the hex block rather than being transferred radially inward toward the heat pipe. To a first order, the measured cartridge heater powers and known geometry can be used as inputs to a 1D radial heat conduction equation to estimate the radial temperature variations in the hex block. During steady-state operation near 1,300–1,400 min, the average power per cartridge heater was in the range of ~55 to 60 W. Conservative assumptions can be made to determine the largest radial difference in temperature. For example, 100% of the 60 W per heater power can be assumed to be dissipated radially outward through a conservatively small area that is 6.35 mm wide (half of the heater diameter) by 279 mm tall (the full height of the hex block). This ignores axial heat losses and heat rejection through the heat pipe, resulting in a maximum heat flux of 33.8 kW/m^2. Dividing this heat flux by an average thermal conductivity of ~23 W/m-K for 300-series SS at these temperatures and multiplying by the ~3 mm radial distance between the embedded TC and the outer surface of the hex block gives an estimated radial temperature difference of 4.4°C. Therefore, the radial variations in temperature were likely negligible at the tested power levels.

Although radial temperature variations appear to have been negligible, there could have been azimuthal temperature variations if the individual heater powers varied significantly. The control system adjusted the power to each cartridge heater so that the temperatures inside the cartridge heaters were equal. There could have been variations in the power required to reach the same internal heater temperature if the BN paste did not provide uniform heat transfer from each heater to the hex block. Figure 13 shows the individual heater powers that were logged while controlling based on the temperatures within the cartridge heaters. Clearly, there is significant variation. For example, near 1,400 min, heater 3 has a power of 65–70 W, whereas heater 4 has a power of ~30–35 W. Azimuthal variations in temperature cannot be easily quantified without instrumenting all faces of the hex block. Future experiments should include additional instrumentation to quantify these temperature variations, but they should also be controlled based on the individual heater power measurements instead of the heater temperatures to ensure a more uniform heat flux throughout the hex block. Alternatively, variable powers could be used to introduce

thermal stresses that might result from nonuniform fission heating in a heat pipe–based microreactor. In either case, the experiment should be controlled based on power instead of temperature.

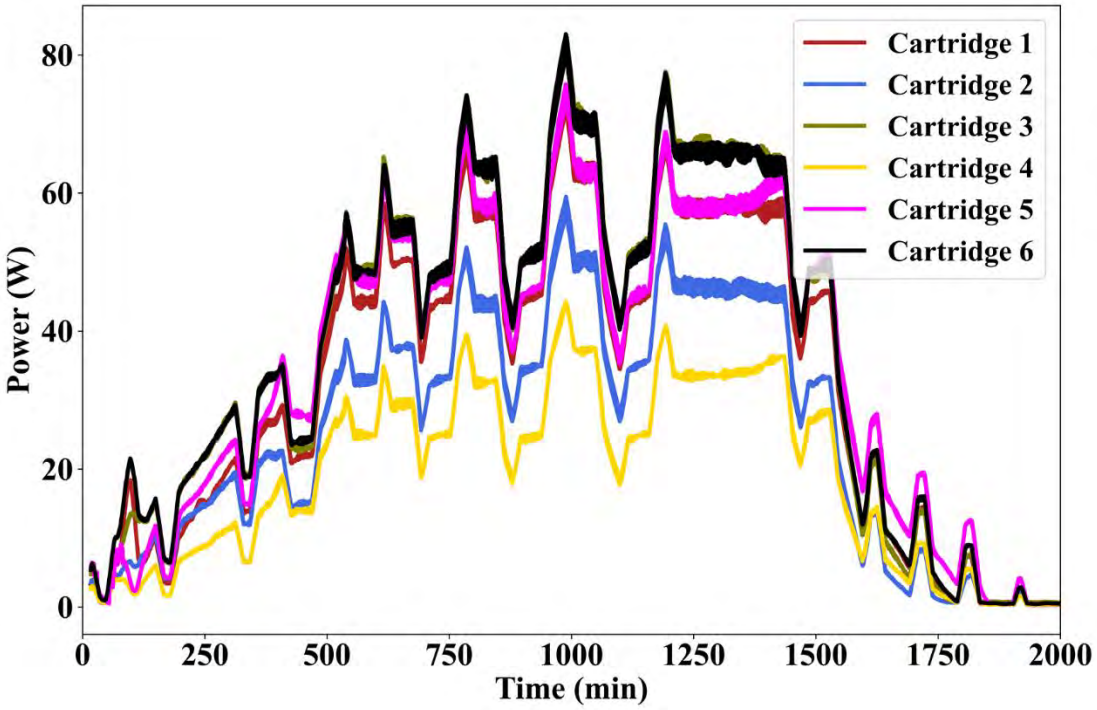

Figure 13. Power supplied to each cartridge heater during the test.

4. SUMMARY

This report discusses the performance of a hex block and Na heat pipe with embedded and surface-mounted sensors during electrical heating in the SPHERE facility. Both Type K TCs and spatially distributed fiber-optic temperature and strain sensors were embedded in a hex block test article. Additional TCs and a high-temperature strain gauge were spot-welded to the surface of the hex block. The SPHERE testing comprised a series of temperature ramps in the range of ~650°C, which is the nominal operating temperature for the Na heat pipe tested in this work. The strain measured by the embedded fiber-optic sensor matched the expected thermal strain that resulted from the difference in thermal expansion between the fiber and the SS304 matrix during the initial temperature ramp. However, the embedded fiber-optic strain sensor broke prematurely at the entrance to the embedded region during this initial ramp. At temperatures <500°C, the strain measured from the resistive strain gauge generally followed the trends of the temperatures measured by the TCs inside the cartridge heaters. However, the strain magnitudes were significantly higher than what would be expected for the expansion of SS304. Furthermore, the measured strain deviated significantly from the measured temperatures once the temperature exceeded ~500°C. The lack of publicly available data on the geometry and materials that comprise the resistive strain gauge make it difficult to understand its response or compensate for the observed drift.

The detailed temperature measurements performed in this experiment enable the temperature distribution within the hex block to be more accurately mapped, which is necessary for determining thermal stresses. The axial temperature distribution was monitored with a nonembedded optical fiber and an array of embedded and nonembedded TCs. The temperature measurements showed significant axial variations in temperature, as evidenced by decreasing temperatures moving axially away from the vertical midplane.

Significant variations in the individual electrical power supplied to each cartridge heater may have also resulted in large azimuthal variations in temperature, but this cannot be confirmed without additional temperature measurements along each face of the hex block. Gas-gap calorimeter measurements showed that the heat pipe rejected only ~20–30% of the total heat, likely because of the large thermal resistance that resulted from the lack of BN paste in between the heat pipe and the hex block. Future heat pipe testing should include the following:

- Additional temperature sensors to better quantify radial, axial, and circumferential temperature distributions within the hex block and heat pipe.
- BN paste or other methods to improve heat transfer between the heat pipe and the hex block and enable testing at higher powers.
- Improved insulation or other methods (e.g., vacuum instead of N_2 backfill) to reduce heat losses.
- Control based on individual cartridge heater electrical powers instead of cartridge heater temperatures.

After implementing these suggestions, the detailed temperature maps could be used with finite element simulations to evaluate differential thermal stresses in the hex block. These stresses are important for understanding the consequences of debonding between a heat pipe and a hex block to ensure that a cascading failure scenario is impossible. Furthermore, a digital twin could predict stresses in real time using feedback from the distributed temperature sensors.

5. REFERENCES

[1] H.R. Trellue, J. O'Brien, R.S. Reid, D. Guillen, P. Sabharwall, "Microreactor Agile Nonnuclear Experimental Testbed Test Plan", Los Alamos National Lab.(LANL), Los Alamos, NM (United States)(2020),

[2] P. Sabharwall, J. Hartvigsen, T. Morton, J. Yoo, S. Qin, M. Song, D. Guillen, T. Unruh, J. Hansel, J. Jackson, "Nonnuclear Experimental Capabilities to Support Design, Development, and Demonstration of Microreactors", *Nucl. Technol.* (2022) 1-19,

[3] J. Yoo, S. Qin, M. Song, J.L. Hartvigsen, Z.D. Sellers, T.J. Morton, P. Sabharwall, J. Hansel, L. Ibarra, B. Feng, "Modeling and Analysis Support for High Temperature Single Heat Pipe Experiment: Current Status and Plan", *Idaho National Laboratory, Idaho Falls, Idaho* (2021) 1-46,

[4] P. Sabharwall, S.M. Bragg-Sitton, C. Stoots, "Challenges in the Development of High Temperature Reactors", *Energy Convers. Manage.* 74 (2013) 574-581, https://doi.org/10.1016/j.enconman.2013.02.021

[5] P.R. Mcclure, D.I. Poston, V.R. Dasari, R.S. Reid, "Design of Megawatt Power Level Heat Pipe Reactors", Los Alamos National Lab.(LANL), Los Alamos, NM (United States)(2015),

[6] C.M. Petrie, N.D.B. Ezell, "Demonstrate Embedding of Sensors in a Relevant Microreactor Component", Oak Ridge National Lab.(ORNL), Oak Ridge, TN (United States)(2020),

[7] K.O. Hill, G. Meltz, "Fiber Bragg Grating Technology Fundamentals and Overview", *J. Lightwave Technol.* 15(8) (1997) 1263-1276, 10.1109/50.618320

[8] S.T. Kreger, D.K. Gifford, M.E. Froggatt, B.J. Soller, M.S. Wolfe, "High Resolution Distributed Strain or Temperature Measurements in Single-and Multi-Mode Fiber Using Swept-Wavelength Interferometry", Optical Fiber Sensors, Optical Society of America, (2006), ThE42,

[9] C.M. Petrie, D.P. Hawn, W. Windl, T.E. Blue, "Reactor Radiation-Induced Attenuation in Fused Silica Optical Fibers Heated up to 1000 C", *Journal of Non-Crystalline Solids* 409 (2015) 88-94,

[10] C.M. Petrie, B. Wilson, T.E. Blue, "In Situ Gamma Radiation-Induced Attenuation in Sapphire Optical Fibers Heated to 1000°C", *J. Am. Ceram. Soc.* 97(10) (2014) 3150-3156, 10.1111/jace.13089

[11] D.P. Hawn, C.M. Petrie, T.E. Blue, W. Windl, "In-Situ Gamma Radiation Induced Attenuation in Silica Optical Fibers Heated up to 600 C", *Journal of Non-Crystalline Solids* 379 (2013) 192-200,

[12] C.M. Petrie, N. Sridharan, "In Situ Measurement of Phase Transformations and Residual Stress Evolution During Welding Using Spatially Distributed Fiber-Optic Strain Sensors", *Meas. Sci. Technol.* 31(12) (2020) 125602,
[13] C.M. Petrie, S. Niyanth, C. Frederick, T. Mcfalls, S. Babu, A. Hehr, M. Norfolk, J. Sheridan, "Embedded Fiber-Optic Sensors for in-Pile Applications", Oak Ridge National Lab.(ORNL), Oak Ridge, TN (United States)(2019),
[14] C.M. Petrie, A. Schrell, D. Leonard, B.C. Jolly, "Demonstration of Embedded Sensors in Ceramic Structures", Oak Ridge National Lab.(ORNL), Oak Ridge, TN (United States)(2020),
[15] C.M. Petrie, N. Sridharan, A. Hehr, M. Norfolk, J. Sheridan, "High-Temperature Strain Monitoring of Stainless Steel Using Fiber Optics Embedded in Ultrasonically Consolidated Nickel Layers", *Smart Mater. Struct.* 28(8) (2019) 085041, ARTN 085041
10.1088/1361-665X/ab2a27
[16] C.M. Petrie, N. Sridharan, M. Subramanian, A. Hehr, M. Norfolk, J. Sheridan, "Embedded Metallized Optical Fibers for High Temperature Applications", *Smart Mater. Struct.* 28(5) (2019) 055012, ARTN 055012
10.1088/1361-665X/ab0b4e
[17] S.Q. Wang, K. Lasn, C.W. Elverum, D. Wan, A. Echtermeyer, "Novel in-Situ Residual Strain Measurements in Additive Manufacturing Specimens by Using the Optical Backscatter Reflectometry", *Addit. Manuf.* 32 (2020) 101040, ARTN 101040
10.1016/j.addma.2020.101040
[18] C. Hensley, K. Sisco, S. Beauchamp, A. Godfrey, H. Rezayat, T. McFalls, D. Galicki, F. List, K. Carver, C. Stover, D.W. Gandy, S.S. Babu, "Qualification Pathways for Additively Manufactured Components for Nuclear Applications", *J. Nucl. Mater.* 548 (2021) 152846, ARTN 152846
10.1016/j.jnucmat.2021.152846
[19] X. Hu, T.G. Lach, K.A. Terrani, "Deuterium Permeation and Retention in 316l Stainless Steel Manufactured by Laser Powder Bed Fusion", *J. Nucl. Mater.* 548 (2021) 152871, https://doi.org/10.1016/j.jnucmat.2021.152871
[20] W.J. Sames, F. List, S. Pannala, R.R. Dehoff, S.S. Babu, "The Metallurgy and Processing Science of Metal Additive Manufacturing", *Int. Mater. Rev.* 61(5) (2016) 315-360,
[21] H. Hyer, R. Newell, D. Matejczyk, S. Hsie, M. Anthony, L. Zhou, C. Kammerer, Y. Sohn, "Microstructural Development in as Built and Heat Treated In625 Component Additively Manufactured by Laser Powder Bed Fusion", *Journal of Phase Equilibria and Diffusion* 42(1) (2021) 14-27, 10.1007/s11669-020-00855-9
[22] D. Havermann, J. Mathew, W.N. MacPherson, R.R. Maier, D.P. Hand, "Temperature and Strain Measurements with Fiber Bragg Gratings Embedded in Stainless Steel 316", *J. Lightwave Technol.* 33(12) (2014) 2474-2479,
[23] R. Zou, X. Liang, Q. Chen, M. Wang, M.A. Zaghloul, H. Lan, M.P. Buric, P.R. Ohodnicki, B. Chorpening, A.C. To, "A Digital Twin Approach to Study Additive Manufacturing Processing Using Embedded Optical Fiber Sensors and Numerical Modeling", *J. Lightwave Technol.* 38(22) (2020) 6402-6411,
[24] H. Hyer, D. Sweeney, C. Petrie, "Characterization of Embedded Sensors in Stainless Steel Test Articles and Design/Planning for Magnet Testing", ; Oak Ridge National Lab. (ORNL), Oak Ridge, TN (United States)(2021),
[25] H.C. Hyer, D.C. Sweeney, C.M. Petrie, "Functional Fiber-Optic Sensors Embedded in Stainless Steel Components Using Ultrasonic Additive Manufacturing for Distributed Temperature and Strain Measurements", *Addit. Manuf.* 52 (2022) 102681, 10.1016/j.addma.2022.102681
[26] A. Hehr, M. Norfolk, "A Comprehensive Review of Ultrasonic Additive Manufacturing", *Rapid Prototyp. J.* (2019),
[27] P. Sabharwall, H. Trellue, J.L. Hartvigsen, T.J. Morton, D.P. Guillen, J.C. Gehin, "Microreactor Program: Experimental Capabilities Summary", Idaho National Lab.(INL), Idaho Falls, ID (United States)(2021),

[28] T.W. Wood, B. Blake, T.E. Blue, C.M. Petrie, D. Hawn, "Evaluation of the Performance of Distributed Temperature Measurements with Single-Mode Fiber Using Rayleigh Backscatter up to 1000c", *IEEE Sens. J.* 14(1) (2014) 124-128, 10.1109/JSEN.2013.2280797
[29] D.C. Sweeney, C.M. Petrie, "Expanding the Range of the Resolvable Strain from Distributed Fiber Optic Sensors Using a Local Adaptive Reference Approach", *Opt. Lett.* 47(2) (2022) 269-272, 10.1364/OL.445245
[30] D.C. Sweeney, A.M. Schrell, C.M. Petrie, "An Adaptive Reference Scheme to Extend the Functional Range of Optical Backscatter Reflectometry in Extreme Environments", *IEEE Sens. J.* 21(1) (2021) 498-509, 10.1109/Jsen.2020.3013121
[31] D.C. Sweeney, D.M. Sweeney, C.M. Petrie, "Graphical Optimization of Spectral Shift Reconstructions for Optical Backscatter Reflectometry", *Sensors* 21(18) (2021) 6154,
[32] J.T. Jones, D.C. Sweeney, A. Birri, C.M. Petrie, T.E. Blue, "Calibration of Distributed Temperature Sensors Using Commercially Available Smf-28 Optical Fiber from 22 °C to 1000 °C", *IEEE Sens. J.* 22(5) (2022) 4144-4151, 10.1109/JSEN.2022.3146185